Biomass Conversion and Biorefinery
https://doi.org/10.1007/s13399-024-05425-4

ORIGINAL ARTICLE

Magnetic nanocomposite synthesized from cocopeat for highly efficient mercury removal from aqueous solutions

Hassan Rezaei[1] · **Negar Movazzaf Rostami**[1] · **Hajar Abyar**[1]

Received: 27 November 2023 / Revised: 5 February 2024 / Accepted: 8 February 2024

Abstract
The utilization of renewable and cost-effective biomass for the production of activated carbon represents an innovative approach to environmental remediation. In this work, environmentally friendly carbon materials derived from cocopeat were employed to create a cocopeat-based magnetic activated carbon (CPAC-Fe_3O_4) nanocomposite for the removal of mercury from aqueous solutions. The CPAC-Fe_3O_4 nanocomposite underwent comprehensive characterization using SEM, FTIR, BET, XRD, and VSM analyses. The optimization process revealed a maximum adsorption capacity of 204.08 mg/g under specific conditions: initial Hg concentration of 20 mg/L, pH of 6, temperature of 25 °C, and adsorbent dose of 0.01 g within 60 min. Isotherm and kinetic modeling exhibited strong agreement with the Freundlich isotherm (0.9749) and pseudo-second-order (0.9997) kinetic models, indicating a favorable chemisorption process. Furthermore, thermodynamic analysis suggested that the adsorption process is endothermic and spontaneous. The adsorption mechanism was elucidated based on FTIR analysis. The results highlight the CPAC-Fe_3O_4 nanocomposite as a promising and sustainable candidate for effective water purification.

Keywords Magnetic nanocomposite · Mercury · Activated carbon · Adsorption · Kinetics

1 Introduction

The water crisis has tremendously increased due to the rapid development in agricultural activities, industrialization, and climate change, threatening the sustainability of ecological systems worldwide [1, 2]. According to the United Nations' report, 2.3 billion people inhabit water-stressed countries [3], which is estimated to substantially upgrade by 2050 [4, 5]. Approximately 4 billion people experience water scarcity for at least 1 month per year, and 2 billion people will suffer from acute water scarcity by 2050 due to water shortage [6, 7]. Therefore, practical approaches are required to deal with water contamination and fulfill sustainable development goals [8–10].

The water quality has deteriorated as a result of heavy metals especially mercury (Hg), which is a priority pollutant due to hindering the enzyme binding sites and disturbing protein synthesis based on the WHO [11] and the US EPA reports [12, 13]. Hg is a neurotoxin and its low vapor pressure intensifies human poisoning [14, 15]. It is ranked second toxic waste by the US Agency for Toxic Substances and Disease Registry [16, 17], and a limit of 2 µg/L Hg^{2+} in drinking water has been established by the US Environmental Protection Agency (USEPA) [15, 18]. Therefore, Hg elimination from water resources and wastewater should receive more attention to avoid its adverse effects on ecosystems and human health.

Despite several accessible techniques for heavy metal removal including ion exchange, reverse osmosis, chemical precipitation, bioremediation, and coagulation, their implementation suffers from byproduct and sludge generation, required time, and cost of operation [19–22]. In the last few decades, researchers have focused on advanced porous materials regarding the exponential increase of nanomaterial demand [23, 24]. Although more than 99% heavy metal removal efficiency can be achieved through the adsorption process [15, 25], the adsorbent properties have fundamental roles in the removal potential. Magnetic nanoparticles have already exhibited special features including large surface

✉ Hassan Rezaei
hassanrezaei@gau.ac.ir

[1] Department of Environmental Sciences, Faculty of Fisheries and Environmental Sciences, Gorgan University of Agricultural Sciences and Natural Resources, Gorgan, Iran

Published online: 16 February 2024

area, high reactivity, selectivity, and catalytic potential. This can be associated with large oxygenated functional groups such as carboxylic, hydroxide, and amide on their surface that facilitate the metal ion bonding through surface complexation and ligand exchange [26]. However, some nanomaterials including $CoFe_2O_4$, $MnFe_2O_4$, and Fe_3O_4 have inherent poor adsorption capacity for heavy metals due to the lack of surface-active functional groups. Zhao et al. [27] believed that their characteristics can be improved using a coating layer of SiO_2 under the outer layer of $CoFe_2O_4$ particles functionalized with polypyrrole. The $CoFe_2O_4$-based core–shell carriers with the grafted group of $-NH_2$ is another proposed ideal adsorbent for Hg with 149.3 mg/g adsorption capacity [28]. Bao et al. [29] also synthesized mercaptoamine-functionalised silica-coated magnetic nanoparticles for the efficient removal of Hg and Pb from wastewater with maximum adsorption capacities of 355 and 292 mg/g, respectively. A novel magnetic diatomite-based material of DMT/$CoFe_2O_4$-p-ATP with an adsorption capability of 213.2 mg/g was also recommended for Hg removal [30]. Kaolin with a high specific surface area and negative charge is appropriate for heavy metal adsorption but easy agglomeration limits its further usage. Therefore, polypyrrole-functionalized magnetic Kaolin was proposed for Hg removal with substantial adsorption capacity of 317.1 mg/g [31].

Although numerous synthesized magnetic nanomaterials for Hg elimination have been proposed, a cost-effective and practical adsorbent with a simple design is indispensable for removing Hg from wastewater. Therefore, the synthesis, characterization, and adsorption efficiency of cocopeat-based magnetic activated carbon (CPAC-Fe_3O_4) nanocomposite were considered, and the following goals were determined: (1) preparation of magnetic nanocomposite using cocopeat; (2) characterization of CPAC-Fe_3O_4 nanocomposite structure and morphology; (3) optimization of Hg removal from aqueous solutions considering the impacts of pH, temperature, contact time, Hg concentration, and adsorbent dosage; and (4) interpretation of adsorption mechanism using isotherm, kinetics, and thermodynamic modeling. Summing up, the results of this study can provide a framework to elaborate cost-effective and promising nanocomposite for industrial wastewater treatment.

2 Materials and methods

2.1 Chemicals

Analytical-grade chemicals were utilized in experimental research. Hg chloride ($HgCl_2$) was used for the preparation of Hg solutions. Iron (II) chloride ($FeCl_2.4H_2O$) and iron (III) chloride ($FeCl_3.6H_2O$) were applied for the magnetization of the adsorbent. Hydrochloric acid (HCl) and sodium hydroxide (NaOH) were also utilized to adjust the pH of the solutions. All chemicals were supplied by the Merck Company.

2.2 *Synthesis of CPAC-Fe_3O_4 nanocomposite*

Cocopeat samples were purchased from a local plant nursery and collected from the fiber separation of coconut husk. A total of 20 g of cocopeat samples was added to deionized water in a 1000-mL flask and heated to 65 °C for 20 min. Then, $FeCl_2.4H_2O$ and $FeCl_3.6H_2O$ with a molar ratio of 2 to 1 were added to the mixture and stirred for 30 min to ensure the diffusion of iron cations to the sample. Afterward, the sample was dehydrated and then transferred to 1 M NaOH solution and heated to 60 °C for 30 min to complete the synthesis of cocopeat-based magnetic nanoparticles. The color of the mixture was changed to black, indicating the successful synthesis of magnetic nanoparticles. The as-synthesized sample was collected and rinsed with deionized water two times to remove impurities and adjust the pH around neutral conditions. Afterward, the samples were dried under sunlight for 48 h, thus powdered and sieved to the size of 60 mesh no. (0.25 mm). The cocopeat samples were further subjected to heating at a rate of 5 °C per minute in a muffle furnace at 600 °C under nitrogen gas with a pressure of 100 mL/min for 2 h.

2.3 Characterization

The elemental analysis was applied by an elemental analyzer (Flash EA 1112, USA), which showed 42% C, 47% O, 6.5% H, 1.5% N, and 3% S contents of cocopeat. The morphology of the CPAC-Fe_3O_4 nanocomposite was analyzed with field emission scanning electron microscopy (FESEM, FEI NOVA NanoSEM 450, Japan). The crystal structure of the CPAC-Fe_3O_4 nanocomposite was determined by X-ray diffractometer (XRD, Ultima, Japan). Fourier-transform infrared spectroscopy (FTIR, Tensor 27, Bruker, Germany) was performed to assess the surface functional groups of the CPAC-Fe_3O_4 nanocomposite. The Brunauer–Emmett–Teller (BET, Belsorp mini II, Microtrac Bel Corp, Japan) method was employed to determine the specific surface area of the synthesized CPAC-Fe_3O_4 nanocomposite. The magnetic properties were measured using the vibrating sample magnetometer (VSM, LBKFB, Kashan Kavir Magnetic Co. Iran).

2.4 Batch adsorption experiment

The adsorption behavior of the CPAC-Fe_3O_4 nanocomposite was evaluated for Hg removal considering the impact of pH, adsorbent dosage, contact time, initial Hg concentration, and temperature. A 1000 mg/L Hg stock solution was prepared

by dissolving the appropriate volume of $HgCl_2$ in deionized water. To determine the optimum condition for maximum Hg removal, the pH of the solution was adjusted on 3, 4, 5, 6, 7, and 8 using 0.1 M HCl and NaOH, while other parameters were constant (0.01 g adsorbent dose, 20 mg/L Hg concentration, and contact time of 60 min at 25 °C). The mixture was shaken at 100 rpm and allowed to react with the magnetic nanocomposite. Then, the CPAC-Fe_3O_4 nanocomposite was removed from the solution by the magnetic field, and the mixture solution was centrifuged (HERMLE Z300, USA) at a rate of 4000 rpm for 5 min and then filtered. A total of 1 mL HNO_3 was further added to the mixture to avoid Hg ions precipitation. The remained Hg concentration in the solution was measured by cold vapor technique with atomic absorption spectroscopy (AAS, Uniam 919). The limit of detection (LOD) for Hg was 0.01 µg/L. The potential of CPAC-Fe_3O_4 nanocomposite was also apprised at Hg concentrations of 5, 10, 20, 50, 70, and 100 mg/L at pH of 6 and 0.01 g adsorbent for 60 min at 25 °C. The same procedure was followed to optimize the contact time at 15, 30, 45, 60, 75, and 90 min at a fixed pH of 6, Hg concentration of 20 mg/L, and 0.01 g adsorbent at 25 °C. Adsorbent doses of 0.01, 0.02, 0.03, 0.04, 0.05, and 0.1 g were considered at a fixed pH of 6 and Hg concentration of 20 mg/L for 60 min at 25 °C. The impact of temperature (15, 20, 25, 30, 35, and 40 °C) was also evaluated at a fixed pH of 6, Hg concentration of 20 mg/L, and 0.01 g adsorbent for 60 min. All experiments were carried out in three replicates.

3 Results and discussion

3.1 *Characterization of CPAC-Fe_3O_4 nanocomposite*

3.1.1 FESEM analysis

The morphology of CPAC-Fe_3O_4 nanocomposite was determined with SEM at 25 keV as depicted in Fig. 1. The activation with NaOH creates cavities with spherical structure, relatively smooth surface, and diameter size of < 100 nm. Several micropores and mesopores are formed, resulting in a high surface area as shown in Fig. 1b and c. Furthermore, the exterior pores facilitate the efficient transport of Hg ions from the aqueous solution to the inner micropores of the CPAC-Fe_3O_4 nanocomposite, increasing the adsorption performance [32]. As can be seen, the CPAC-Fe_3O_4 nanocomposite manifests various pore sizes with relatively uniform distribution. The large size of pores in the raw cocopeat sample and small pores in the cocopeat conversion to activated carbon were also reported by Varghese et al. [33]. The SEM image after Hg adsorption shows the vaccine sites on the surface of the CPAC-Fe_3O_4 nanocomposite, indicating a high potential of adsorbent to multiple adsorb Hg ions in a batch system (Fig. 1d).

3.1.2 FTIR analysis

The synthesized CPAC-Fe_3O_4 nanocomposite was analyzed by FTIR spectroscopy to determine the effective functional groups in the adsorption process. Figure 2 manifests the FTIR spectra for synthesized CPAC-Fe_3O_4 nanocomposite before and after Hg removal. A broad peak at 3434.21 cm^{-1} is attributed to the stretching vibrations of the O–H band [26, 34, 35]. A peak at 2922.56 cm^{-1} corresponds to C-H SP^3 stretching, which verifies the presence of alkanes in the nanocomposite. Strong peaks at 1733.21 cm^{-1} and 1639.45 cm^{-1} can be ascribed to stretching of C = O [36]. Moreover, the absorption at 1200–1600 cm^{-1} is due to CH_2 and CH_3 stretching. A peak at 841.06 cm^{-1} can be associated with the stretching vibration of C-O. Absorption peaks at 618.62 cm^{-1} and 522.94 cm^{-1} correspond to the Fe–O band [36, 37], evidence of the formation of magnetic nanocomposite (Fig. 2a). Therefore, the presence of hydroxyl, carboxylic acid, and lactones functional groups on the surface of CPAC-Fe_3O_4 nanocomposite plays the main role in Hg ion adsorption. The changes in the vibrational spectra at 681.71, 747.42, 804.10, and 1077.28 cm^{-1} confirmed the adsorption of Hg ions by the functional groups (Fig. 2b).

3.1.3 XRD analysis

X-ray diffraction is a practical technique for investigating the characteristics of the crystal structure, such as the qualitative features of unknown materials, lattice geometry, crystal phase, crystal size, single crystal orientation, and lattice defects [38]. To determine the crystalline phase of the CPAC-Fe_3O_4 nanocomposite, XRD analysis was performed in the range of angle $2\theta = 0$–80° and temperature 25 °C. Regarding Fig. 3, the peaks at $2\theta = 30.12°$ and 35.36° reveal the crystalline phase, with 100% purity and maximum intensity of 141 at 36.36°. Based on the obtained spectrum, 6 peaks at $2\theta = 35.4°$, 39.36°, 43.16°, 53.6°, 56.84°, 64.48° in inverse cubic spinel confirm the presence of Fe_3O_4 nanoparticles on the CPAC-Fe_3O_4 nanocomposite [39]. In addition, the obtained peaks are compatible with the standard peak (No JCPDS. 19-0629) and prove the existence of magnetic activated carbon and Fe_3O_4 particles.

3.1.4 BET analysis

The BET theory is based on a simplified model of physisorption and determines a specific surface area of adsorbent by nitrogen sorption–desorption measurement at a constant temperature of liquid nitrogen (77 K) [40]. The pore size distribution was achieved by the Barrett-Joyner-Halenda

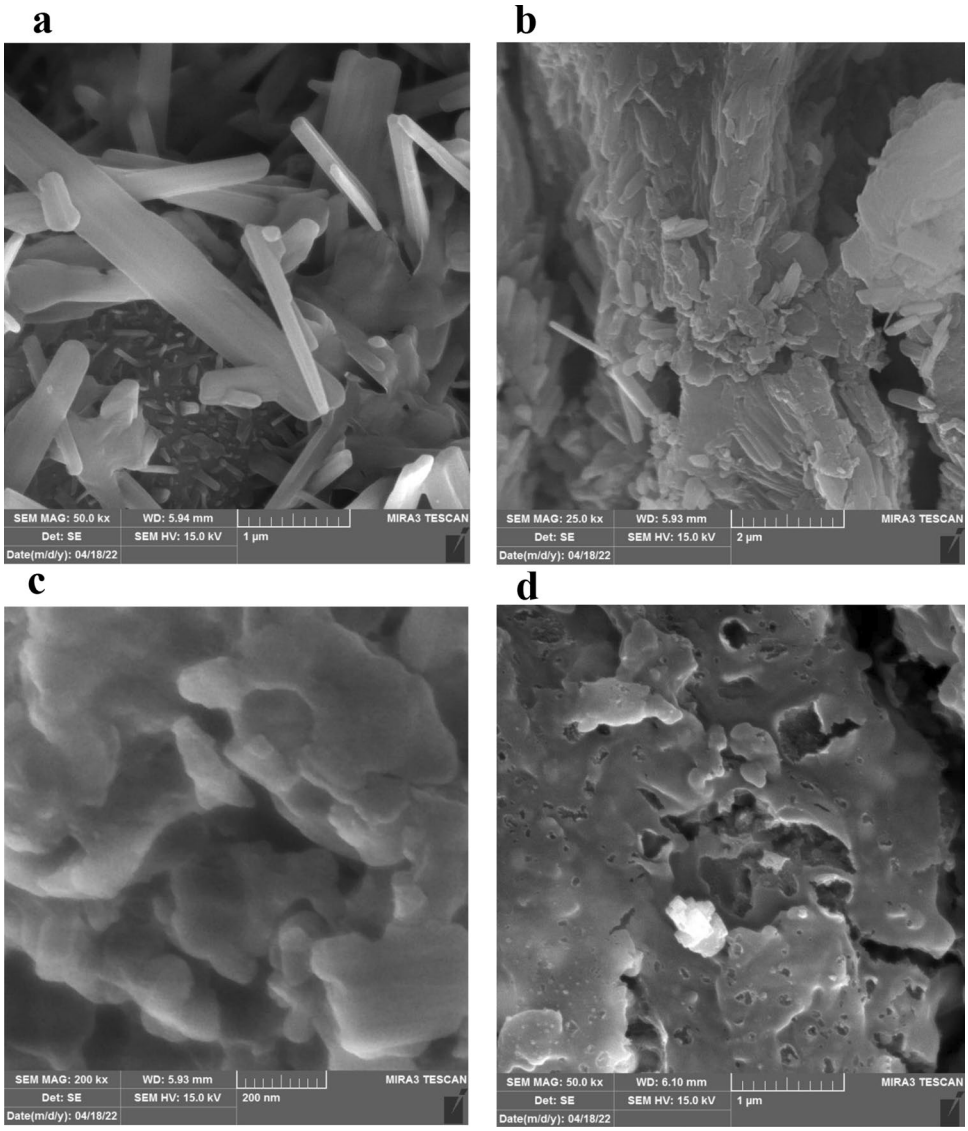

Fig. 1 FESEM images of cocopeat fiber (**a**) and CPAC-Fe_3O_4 nanocomposite before (**b**, **c**) and after (**d**) Hg removal

(BJH) equation during the desorption phase. The BJH method attributes the relative pressure of nitrogen in equilibrium with the porous adsorbent to the size of the pores, considering the Kelvin equation [41]. The pore size radii which are covered by the BJH calculations ranged from 1.7 to 300 nm [42]. The results of the BET analysis of the CPAC-Fe_3O_4 nanocomposite revealed that the size of the nanopores was around 2.27 nm, and the total volume was 0.067 cm^3/g of the CPAC-Fe_3O_4 nanocomposite (Table 1). The specific surface area of the prepared nanocomposite was also equal to 118.25 m^2/g. The volume of required gas to create a single layer on the CPAC-Fe_3O_4 nanocomposite was estimated as 27.168 cm^3/g. Notably, the high surface area of the nanocomposite indicates a suitable substrate for bonding with Fe_3O_4 nanoparticles. The shape of the adsorption/desorption isotherms might be included in type IV based on the International Union of Pure and Applied Chemistry (IUPAC), with a hysteresis loop, which showed the porosity of activated carbon (Fig. 4). A lower p/p_0 ratio depicted narrow and micropores, raising the agglomeration of Hg ions and adsorption efficiency [43, 44].

3.1.5 VSM analysis

Figure 5 illustrates the magnetization curves of Fe_3O_4 and the CPAC-Fe_3O_4 nanocomposite at room temperature and − 10,000 to 10,000 oersted (Oe) field. The saturation values for Fe_3O_4 particles and the CPAC-Fe_3O_4 nanocomposite are 63.77 (Fig. 5a) and 2.5 (Fig. 5b) emu/g, respectively, and have an S-like form. The decrease of magnetization properties in the CPAC-Fe_3O_4 nanocomposite was attributed to the existence of nonmagnetic particles. Moreover, the CPAC-Fe_3O_4 nanocomposite follows the behavior pattern of superparamagnetic materials and has no hysteresis

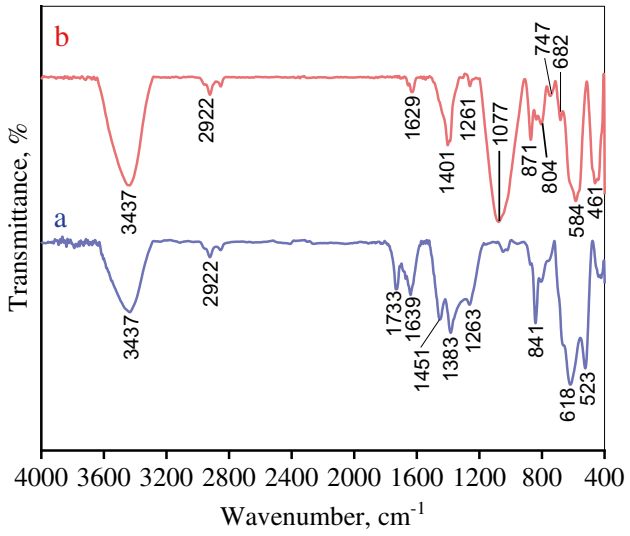

Fig. 2 FTIR spectra of CPAC-Fe_3O_4 nanocomposite before (a) and after (b) Hg removal

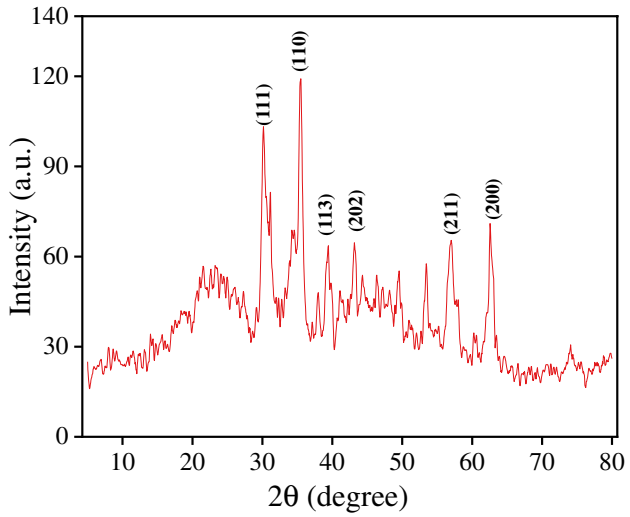

Fig. 3 XRD profile of the CPAC-Fe_3O_4 nanocomposite

loop [45]. Therefore, the magnetization curve passes through the origin, implying no coercive field and remanent magnetization. The curve primarily moves away from the center with an almost constant slope. It indicates that the relationship between magnetization and the magnetic field is linear. Then, the slope of the curve gradually begins to reduce and the acceleration of magnetization decreases to reach saturation magnetization. After that, increasing the applied external magnetic field density does not affect enhancing the magnetization, and the magnetic material is completely saturated.

3.2 Effect of pH

Figure 6a illustrates the adsorption efficiency of Hg ions on the CPAC-Fe_3O_4 nanocomposite. As the pH of the solution was increased from 3 to 6, the Hg adsorption enhanced from 101.8 to 182.4 mg/g with a maximum removal rate of 91.2%. Whereas, a further increase in pH to 8 led to a 14.97% reduction in Hg removal. The functional groups such as carboxyl and amino groups are protonated at low pH causing the electrostatic repulsion between the functional groups and positively charged Hg ions and subsequently hindering the adsorption [35, 46]. However, the increase in pH deprotonates the functional groups and the Hg species (Hg (II), $Hg(OH)^+$, and $Hg(OH)_2$) can chelate with the neutral functional groups, leading to high adsorption [35, 46]. Einollahipeer and Okati [47] also referred to a strict competition between Hg^{2+} and H_3O^+ at low pH accompanied by HgOH formation at pH higher than 7 with a lower affinity towards amine grafted magnetic graphene oxide (m-GO-NH_2), which could reduce the Hg adsorption [48]. The formation of a colloidal precipitate at higher pH was also attributed to lower adsorption efficiency [35]. Ge et al. [49] highlighted the increasing trend of Hg removal with a pH increase to 6, using poly(itaconic acid)-grafted crosslinked chitosan nanoadsorbent. Similar results were reported in the literature [50, 51].

3.3 Effect of Hg concentration

The effect of Hg concentration in the range of 5 to 100 mg/L at pH 6 is exhibited in Fig. 6b. The maximum removal efficiency (98.3%) was observed at 5 mg/L, which was decreased to 91.2% at a concentration of 20 mg/L. A further increase to 94.8% was detected at a concentration of 50 mg/L, while reduced to 90.21% at 100 mg/L concentration. A reduction in Hg adsorption at high Hg concentration can be related to the repulsive force between adsorbed Hg ions and the remaining ones in the solution due to limited available sites on the adsorbent [52, 53]. In contrast, at low Hg concentrations, the adsorption occurs on high-energy

Table 1 Physical characteristics of the CPAC-Fe_3O_4 nanocomposite

Sample	S_{BET} m^2/g	V_{mic} cm^3/g	V_{mes} cm^3/g	V_{total} cm^3/g	V_{mic}, %	$R_{(PD*)}$ nm
CPAC-Fe_3O_4	118.25	0.041	0.026	0.067	61.19	2.27

*Pore diameter (PD)

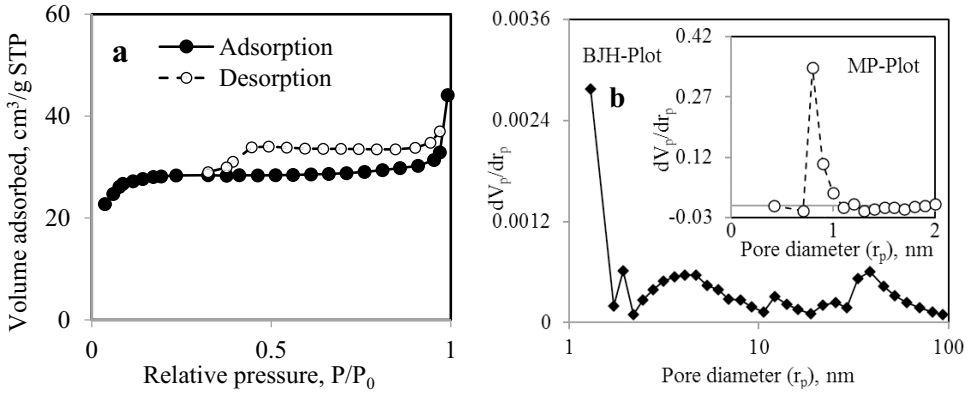

Fig. 4 N_2 adsorption/desorption isotherms (**a**) and BJH pore size distribution and MP plot (**b**)

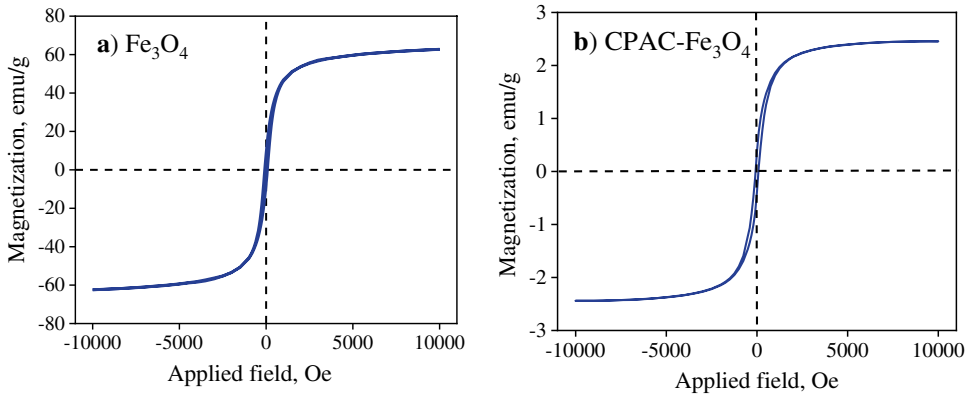

Fig. 5 VSM magnetization curve of Fe_3O_4 (**a**) and CPAC-Fe_3O_4 nanocomposite (**b**)

sites on the adsorbent [15]. The adsorption capacity was also increased from 49.15 to 902.15 mg/g in parallel with the increase in initial Hg concentration. This can be ascribed to the interaction between adsorption sites and Hg ions, which can diffuse the adsorption sites rapidly until all are fully occupied and equilibrium occurs [54]. The obtained adsorption capacity in this study was higher than that for Pistachio-nut/licorice residues (147.1 mg/g) [55], curcumin-based biocomposite (144.9 mg/g) [56], and carboxymethyl CS-sewage sludge (594 mg/g) [57].

3.4 Effect of adsorbent dose

The adsorbent dose as a critical and effective parameter in the adsorption process was investigated. As shown in Fig. 6c, the common pattern is that the increase in adsorbent dose resulted in more Hg ion removal and then decreased when the adsorbent dose exceeded a threshold. Notably, even in the lowest adsorbent dose (0.01 g), substantial removal efficiency was achieved (91.2%). The increase in nanocomposite dose from 0.01 to 0.03 g revealed a 4.3% enhancement in adsorption efficiency. This can be justified by more available active binding sites on the surface of the adsorbent [58]. A further reduction to 88.3% was attained at 0.1 g adsorbent dose. The adsorption capacity was decreased from 182.4 (0.01 g dosage) to 17.66 mg/g (0.1 g dosage), which was because of more vacant sites at higher doses of adsorbent [59].

3.5 Effect of contact time

Adsorption is a time-dependent process and prediction of the removal rate of Hg ions is indispensable to optimize the process in the full-scale operation. Figure 6d illustrates the increase in adsorption efficiency and capacity when the contact time was upgraded from 15 (71.7%) to 90 min (96.07%). It is interesting to mention that a rapid increase in Hg removal at the initial time is relevant to a greater number of available active sites, which gradually are occupied with time increasing [60, 61]. Moreover, the adsorption is controlled through the diffusion process from the solution to the adsorbent surface, which is slowed down due to fewer available adsorption sites [62]. Regarding literature [47], the capability of m-GO-NH_2 to adsorb Hg ions displayed a rise from 79.02 to 95.54%, while the contact time was increased from 15 to 90 min. Another study revealed 60% Hg removal by Fe_3O_4@SiO-NH-COOH in 5 min and reached 75% after 1 h [63]. The highest adsorption capacity in the present study was 192.15 mg/g at 90 min, higher than reported values as 157.9 mg/g in 60 min [64] and 118.55 mg/g in 180 min [65],

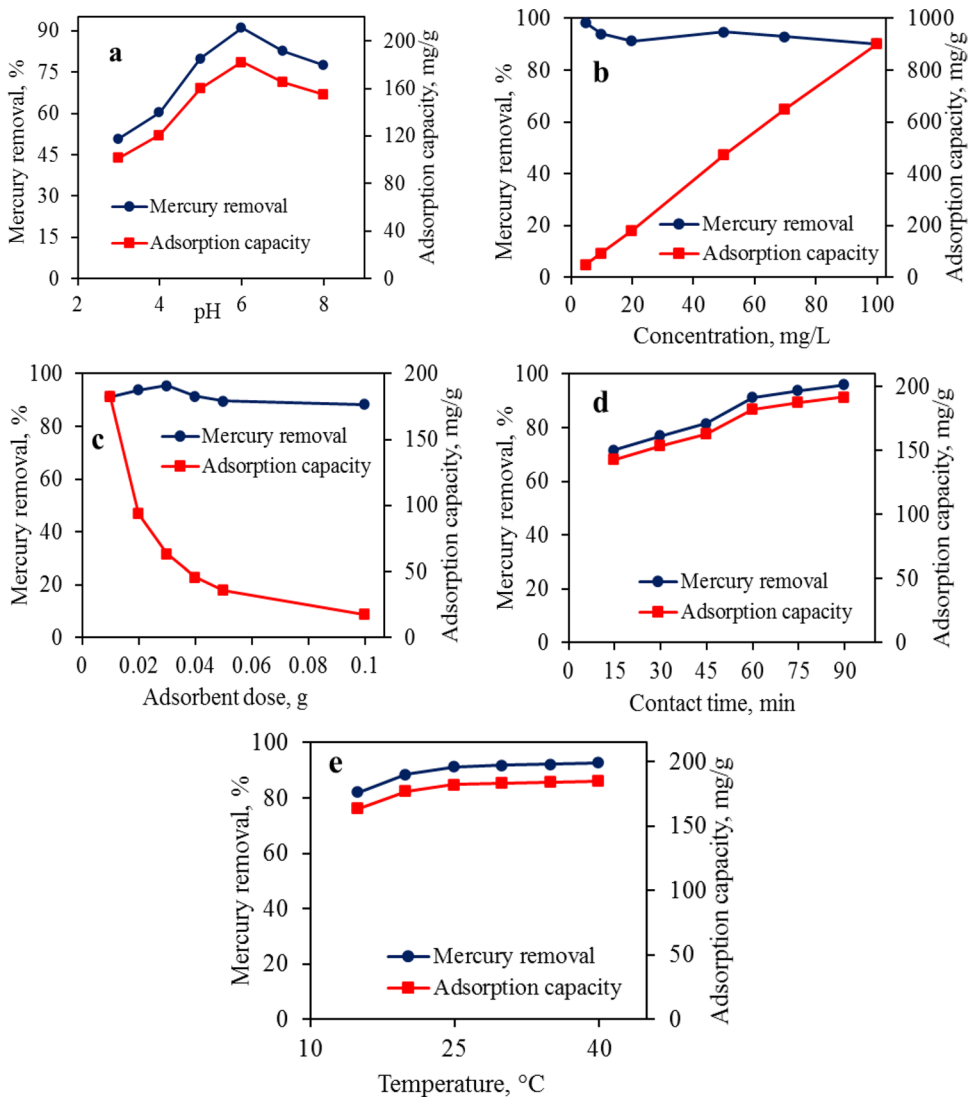

Fig. 6 The impacts of operational parameters on Hg removal. pH (**a**), Hg concentration (**b**), adsorbent dose (**c**), contact time (**d**), and temperature (**e**)

highlighting the potential of the CPAC-Fe_3O_4 nanocomposite in Hg ion adsorption.

3.6 Effect of temperature

The increase in the temperature of a solution from 15 to 40 °C enhanced the removal efficiency in the range of 82.07 to 92.67% alongside the adsorption capacity from 164.15 to 185.35 mg/g (Fig. 6e). The temperature enhancement decreases the solution viscosity and accelerates the diffusion of Hg ions into the adsorbent, rapidly occupying the surface of the adsorbent in a shortened time [66, 67]. It should be noticed that the excessive mobility of the metal ions at high temperatures could lessen their accessibility and lower removal efficiency [15]. Although the most common optimal temperature for the adsorption process is an ambient temperature (25 °C), however, various temperature values were also reported. The adsorption capacity of the FeCu-based biochar was as high as 3901 ng/g at an optimal adsorption temperature of 200 °C [68]. The highest adsorption capacity of coconut pith-based char [69] was also achieved at 50 °C (2395.98 µg/g) for an initial Hg concentration of 200 µg/m^3. Another study referred to a temperature of 150 °C for maximum Hg removal (120 µg/g) using sunflower husk-based char [70].

3.7 Adsorption isotherms and kinetics

The degree of pollutant adsorption onto the surface of the adsorbent commonly depends on the equilibrium concentration in the aqueous solution and temperature, while at a constant temperature, the adsorption capacity (q_e) mainly relates to the final pollutant concentration (C_e) [2, 71]. Hence, Langmuir and Freundlich isotherm models were assessed to determine the Hg adsorption mechanism of the CPAC-Fe_3O_4 nanocomposite. Table 2

Table 2 Isotherm, kinetics, and thermodynamic study of the adsorption process and comparison with other adsorbents for Hg removal

Isotherm	Langmuir			Freundlich					
Equation	$\frac{C_e}{q_e} = \frac{1}{q_m b} + \frac{1}{q_m} C_e$			$lnq_e = lnK_F + \frac{1}{n} lnC_e$					
Adsorbent	q_{max} (mg/g)	b (L/mg)	R^2	K_F (mg/g)(L/mg)$^{1/n}$		n		R^2	Reference
CPAC-Fe_3O_4	3333.3	0.187	0.7469	434.85		1.408		0.9749	This study
THS-DES@M-GO	215.1	8.111	0.992	176.1		12.73		0.871	[19]
Fe_3O_4-xGO	181.8	1.058	0.9554	76.44		2.271		0.9433	[65]
Imino-IGO	247.52	0.039	0.992	48.375		3.58		0.945	[52]
m-GO-NH_2	90.90	1.51	0.913	2.73		0.0013		0.972	[47]
$CoFe_2O_4$-rGO	157.9	0.2372	0.9752	25.42		1.481		0.9574	[64]
Kinetic	Pseudo-first order			Pseudo-second order					
Equation	$\ln(q_e - q_t) = lnq_e - k_1 t$			$\frac{t}{q_t} = \frac{1}{k_2 q_e^2} + \frac{1}{q_e} t$					
Adsorbent	q_e (mg/g)	k_1 (min^{-1})	R^2	q_e (mg/g)		k_2 (g/mg min)		R^2	Reference
CPAC-Fe_3O_4	69.45	0.009	0.3579	204.08		0.0011		0.9997	This study
Fe_3O_4-xGO	57.61	0.0184	0.7693	119.05		0.0027		0.9989	[65]
Coconut pith chars	6.067	60	0.94	6.067		1.4×10^{-14}		0.98	[69]
m-GO-NH_2	57.35	0.0251	0.9244	108.69		0.00094		0.9975	[47]
CMNC	114.8	0.063	0.995	144.9		0.00053		0.98	[56]
Zeolite-Ag_2S	165	0.0004	0.793	256.4		0.00004		0.995	[75]
Thermodynamic	$lnK_c = \frac{\Delta S}{R} - \frac{\Delta H}{RT}$			$\Delta G = -RTlnK_c$					
ΔH (kJ/mol)	ΔS (kJ/mol K)			ΔG (kJ/mol)					
42.94	0.165			288 K	293 K	298 K	303 K	308 K	313 K
				−3.64	−4.99	−5.79	−6.07	−6.32	−6.60

demonstrates the isotherm equations accompanied by the constant values and maximum adsorption capacity. The fitting results derived from the isotherm modeling are depicted in Fig. 7. As can be seen, the Freundlich isotherm model gave the highest R^2 (0.9749) with a K_F value of 434.85 mg/g (l/mg)$^{1/n}$, fitting well with the empirical data. The isotherm results confirmed the multilayer adsorption of Hg ions and the heterogeneous surface of the CPAC-Fe_3O_4 nanocomposite [34, 52]. The value of 1/n in the Freundlich isotherm model was less than 1, indicating the desirable adsorption of Hg ions [47]. Bhatnagar et al. [72] modified pectin and cellulose composites with cocopeat biochar and SDS and highlighted the best fit with Freundlich isotherm, which showed multilayer chemisorption via complexation. The pseudo-first-order and pseudo-second-order kinetic models were employed to further analyze the adsorption kinetic (Table 2). The determination coefficient values demonstrated a better fit of empirical data with the pseudo-second-order kinetic model ($R^2 = 9997$), manifesting that the adsorption of Hg ions through the CPAC-Fe_3O_4 nanocomposite followed a chemisorption process [73] as depicted in Fig. 7d. The q_e value was 204.08 mg/g, higher than that reported in the literature [35, 56]. Sireesha and Sreedhar [32] noted that the chromium adsorption mechanism of H_3PO_4 surface-modified cocopeat biochar (PSMCB) was chemisorption and followed a pseudo-second-order kinetic model.

3.8 Thermodynamic studies

The CPAC-Fe_3O_4 nanocomposite performance in Hg removal was investigated at different temperatures (288, 293, 298, 303, 308, and 313 K). The enthalpy (ΔH) and entropy (ΔS) were estimated from the slope and intercept of 1/T versus lnK_c. Gibbs free energy (ΔG) was also calculated using the equation in Table 2. The negative values of ΔG presented the spontaneous nature of Hg adsorption [35]. Moreover, the increase in temperature from 288 to 313 K decreased the ΔG value from − 3.643 kJ/mol to − 6.604 kJ/mol, implying the endothermic adsorption of Hg ions. The positive and high value of ΔH verified the endothermic adsorption process and strong interaction between Hg ions and adsorbent [65]. The positive value of ΔS also presented the randomness adsorption of Hg ions due to the interference of water molecules in the solution [52, 74].

3.9 Comparison with other adsorbents

Table 3 compares the CPAC-Fe_3O_4 nanocomposite efficiency with other synthesized adsorbents for Hg removal. As can be

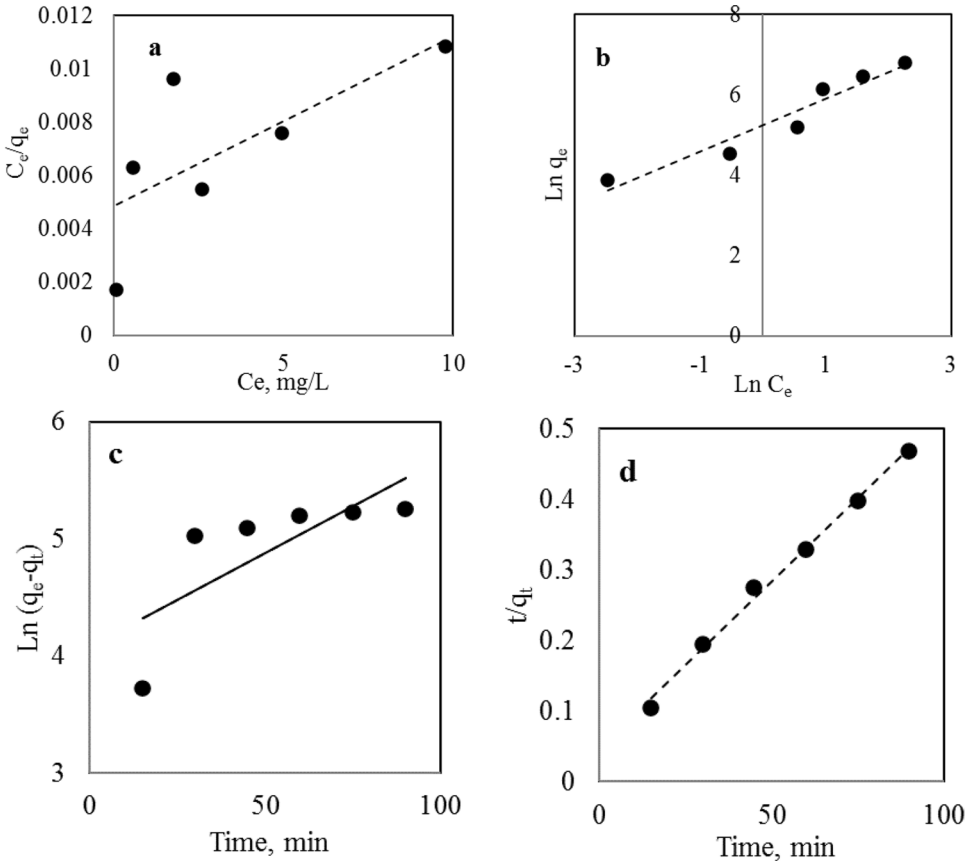

Fig. 7 Langmuir (**a**) and Freundlich (**b**) isotherm models and pseudo-first-order (**c**) and pseudo-second-order (**d**) kinetic models

seen in Table 3, more than 94% Hg removal was achieved for the various applied adsorbents, whereas a significant distinction was observed in adsorption capacity. Arshadi et al. [76] manifested the maximum adsorption efficiency of 3232 mg/L for Hg removal by a novel heterogeneous nanodendrimer. They increased the removal capacity through several pretreatment processes and heterogenized l-cysteine methyl ester dendrimer on the surface. A lower adsorption capacity was also reported for Hg removal due to differences in adsorbent characteristics and operational conditions [71, 77]. However, it is worth mentioning that the CPAC-Fe_3O_4 nanocomposite could remove 71.7% of Hg ions within 15 min, indicating the significant potential of the synthesized adsorbent. On the other hand, the maximum adsorption capacity was substantially higher than that of other adsorbents. Furthermore, the CPAC-Fe_3O_4 nanocomposite underlined high stability after 13 cycles with more than 80% Hg removal (Fig. 8). Therefore, the CPAC-Fe_3O_4 nanocomposite is recommended to be applied for Hg removal due to its simplicity, high potential, and low cost.

Table 3 Comparison of Hg adsorption potential of synthesized adsorbents

Adsorbent	Adsorption time, (min)	Hg concentration, (mg/L)	Adsorption capacity, (mg/g)	Removal, (%)	Reference
CPAC-Fe_3O_4	60	20	204.08	98	This study
Fe_3O_4@ThioG-LDH	540	1000	480.69	94.98	[78]
Fe_3O_4@SiO_2@Se	20	5	70.42	99.07	[71]
Imino-IGO	120	10	230	100	[52]
Modified mixed-oxides	6	-	3232	>97.5	[76]
THS-DES@M-GO	30	30	215.1	99.9	[19]
Fe_3O_4-xGO	180	-	118.54	94.5	[65]
Camellia oleifera shell biochar	1440	1	57.6	97.2	[77]

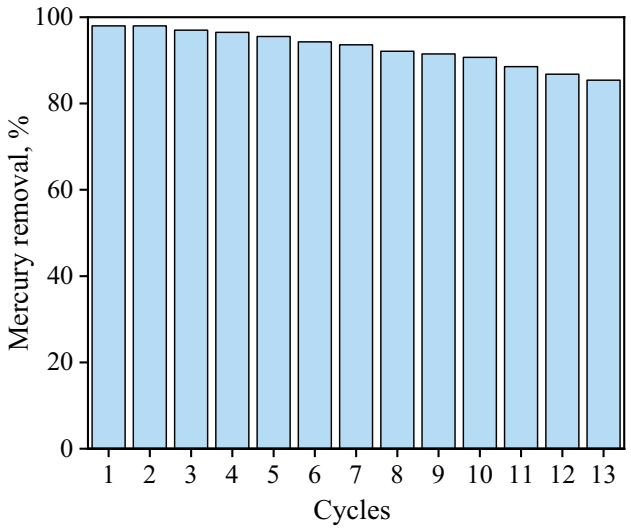

Fig. 8 Reusability of CPAC-Fe_3O_4 nanocomposite

3.10 Adsorption mechanism

Various forms of Hg such as Hg^{2+}, $HgOH^+$, $HgCl^+$, and $Hg(OH)_2$ are present in an aqueous solution under pH < 3. The formation of Hg^{2+} is observed with pH enhancement and further dissolved $Hg(OH)_2$ at pH higher than 6 [27]. When the pH of the solution increases more than 4, H_3O^+ ions decrease and more ionized functional groups are formed [79]. Oxygen functional groups such as carboxyl and carbonyl groups significantly contribute to mercury adsorption [80]. The reaction of Hg ions and these functional groups leads to the formation of surface complexes on the adsorbent surface. The chemical reactions are as follows [55]:

$$C_xOH^{2+} + Hg^{2+} \rightarrow C_xOHg^{2+} + 2H^+ \quad (1)$$

$$2C_xOH^{2+} + Hg^{2+} \rightarrow (C_xO)_2Hg^{2+} + 2H^+ \quad (2)$$

The role of the surface chemistry of CPAC-Fe_3O_4 nanocomposite on the adsorption mechanism was assessed using FTIR. The peaks at 1639.45 and 1733.21 cm^{-1} ascribed to the C = O group changed after the Hg adsorption and a new peak at 1629 cm^{-1} appeared, which was associated with O-Hg. A sharp peak at 841.62 cm^{-1} also decreased after adsorption, indicating chemisorbed C-O group contribution [81].

4 Conclusion

The application of low-cost and eco-friendly CPAC-Fe_3O_4 nanocomposite derived from cocopeat, a by-product of coconut husk processing, was apprised for Hg removal from aqueous solution. The CPAC-Fe_3O_4 nanocomposite illustrated spherical morphology with an average pore diameter of 2.27 nm. The saturation magnetization value was 2.5 emu/g, confirming the appropriate magnetic properties of the synthesized nanocomposite. The equilibrium adsorption capacity of the CPAC-Fe_3O_4 nanocomposite was 204.08 mg/g with a substantial Hg removal efficiency of 98%. The empirical data was well fitted with pseudo-second-order kinetic and the Freundlich isotherm models. In addition, Hg adsorption was endothermic and spontaneous based on thermodynamic study. It can be concluded that the CPAC-Fe_3O_4 nanocomposite can be an eco-friendly candidate with a noticeable capability for Hg removal.

Author contribution Hassan Rezaei: conceptualization, investigation, methodology, and supervision; Negar Movazzaf Rostami: investigation, methodology, original draft; Hajar Abyar: data analysis, original draft, and draft review and editing.

Funding This work was supported by Gorgan University of Agricultural Sciences and Natural Resources, Iran [grant number 01–474-96].

Data availability Not applicable.

Declarations

Ethics approval and consent to participate Not applicable.

Competing interests The authors declare no competing interests.

References

1. Abyar H, Nowrouzi M, Rostami A (2022) A comprehensive study of biological phosphorus removal systems from economic and environmental perspectives based on the optimization approach. Environ Technol Innov 28:102811
2. Nowrouzi M, Abyar H, Rohani S (2023) A comparison of nitrogen removal systems through cost-coupled life cycle assessment and energy efficiency analysis. Sci Total Environ 858:159787
3. J Rajapakse M Otoo G Danso 2023 Progress in delivering SDG6: safe water and sanitation Cambridge Prisms: Water 1 e6
4. Barati AA, Pour MD, Sardooei MA (2023) Water crisis in Iran: a system dynamics approach on water, energy, food, land and climate (WEFLC) nexus. Sci Total Environ 882:163549
5. AMMA Caretta, RBM Arfanuzzaman, SMR Morgan, M Kumar Water. In: Climate change 2022: impacts, adaptation, and vulnerability. Contribution of Working Group II to the in: I.P.o.C. Change (Ed.) 2022
6. He C, Liu Z, Wu J, Pan X, Fang Z, Li J, Bryan BA (2021) Future global urban water scarcity and potential solutions. Nat Commun 12(1):4667
7. Mekonnen MM, Hoekstra AY (2016) Four billion people facing severe water scarcity. Sci Adv 2(2):e1500323
8. Dixit A, Madhav S, Mishra R, Srivastav AL, Garg P (2022) Impact of climate change on water resources, challenges and mitigation strategies to achieve sustainable development goals. Arab J Geosci 15(14):1296

9. Mikulčić H, Baleta J, Wang X, Duić N, Dewil R (2022) Sustainable development in period of climate crisis. J Environ Manage 303:114271
10. Stringer LC, Mirzabaev A, Benjaminsen TA, Harris RM, Jafari M, Lissner TK, Stevens N, Tirado-von Der Pahlen C (2021) Climate change impacts on water security in global drylands. One Earth 4(6):851–864
11. Attari M, Bukhari SS, Kazemian H, Rohani S (2017) A low-cost adsorbent from coal fly ash for mercury removal from industrial wastewater. J Environ Chem Eng 5(1):391–399
12. Monjane-Mabuie A, Mondlane-Milisse A, Pedro O, Leão-Buchir J, Correia D (2022) Mercury pollution assessment and metallothionein gene expression in tilapia (Oreochromis mossambicus): a case study of Revuè River in Manica, Mozambique. Rendiconti Lincei Scienze Fisiche e Naturali 33(3):513–526
13. Zarei S, Raanaei H, Niad M (2023) Investigation of mercury removal by Fe_3O_4@ SiO_2-NH_2-GO-NC as magnetic nanocomposite. Inorg Chem Commun 152:110665
14. Adibkia M, Tajjarod S, Talavari A, Noviery E, Azimi Maleki S (2017) The effect of amino acid coating on the performance of magnetic nanoparticles for the elimination of mercury from waste. Chem Metall Eng J 4(1):1–11
15. EC Emenike, AG Adeniyi, KO Iwuozor, CJ Okorie, AU Egbemhenghe, PE Omuku, KC Okwu, OD Saliu 2023 A critical review on the removal of mercury (Hg^{2+}) from aqueous solution using nanoadsorbents Environ Nanotechnol Monit Manag 100816
16. Behjati M, Baghdadi M, Karbassi A (2018) Removal of mercury from contaminated saline wasters using dithiocarbamate functionalized-magnetic nanocomposite. J Environ Manage 213:66–78
17. EC Emenike, KO Iwuozor, SU Anidiobi Heavy metal pollution in aquaculture: sources, impacts and mitigation techniques Biol Trace Elem Res (2021) 1–17
18. Awual MR (2017) Novel nanocomposite materials for efficient and selective mercury ions capturing from wastewater. Chem Eng J 307:456–465
19. Chen J, Wang Y, Wei X, Xu P, Xu W, Ni R, Meng J (2018) Magnetic solid-phase extraction for the removal of mercury from water with ternary hydrosulphonyl-based deep eutectic solvent modified magnetic graphene oxide. Talanta 188:454–462
20. Igwegbe CA, Obiora-Okafo IA, Iwuozor KO, Ghosh S, Kurniawan SB, Rangabhashiyam S, Kanaoujiya R, Ighalo JO (2022) Treatment technologies for bakers' yeast production wastewater. Environ Sci Pollut Res 29(8):11004–11026
21. Iwuozor KO (2019) Prospects and challenges of using coagulation-flocculation method in the treatment of effluents. Adv J Chem A 2(2):105–127
22. Saleh TA, Mustaqeem M, Khaled M (2022) Water treatment technologies in removing heavy metal ions from wastewater: a review. Environ Nanotechnol Monit Manag 17:100617
23. Talebi J, Halladj R, Askari S (2010) Sonochemical synthesis of silver nanoparticles in Y-zeolite substrate. J Mater Sci 45:3318–3324
24. Yaqoob AA, Ahmad H, Parveen T, Ahmad A, Oves M, Ismail IM, Qari HA, Umar K, Mohamad Ibrahim MN (2020) Recent advances in metal decorated nanomaterials and their various biological applications: a review. Front Chem 8:341
25. Nejati B, Adami P, Bozorg A, Tavasoli A, Mirzahosseini AH (2020) Catalytic pyrolysis and bio-products upgrading derived from Chlorella vulgaris over its biochar and activated biochar-supported Fe catalysts. J Anal Appl Pyrol 152:104799
26. Nowrouzi M, Younesi H, Bahramifar N (2017) High efficient carbon dioxide capture onto as-synthesized activated carbon by chemical activation of Persian Ironwood biomass and the economic pre-feasibility study for scale-up. J Clean Prod 168:499–509
27. Zhao Y, Xia K, Zhang Z, Zhu Z, Guo Y, Qu Z (2019) Facile synthesis of polypyrrole-functionalized $CoFe_2O_4$@ SiO_2 for removal for Hg (II). Nanomaterials 9(3):455
28. Wang X, Zhang Z, Zhao Y, Xia K, Guo Y, Qu Z, Bai R (2018) A mild and facile synthesis of amino functionalized $CoFe_2O_4$@ SiO_2 for Hg (II) removal. Nanomaterials 8(9):673
29. Bao S, Li K, Ning P, Peng J, Jin X, Tang L (2017) Highly effective removal of mercury and lead ions from wastewater by mercaptoamine-functionalised silica-coated magnetic nano-adsorbents: behaviours and mechanisms. Appl Surf Sci 393:457–466
30. Zhang S, Qian L, Zhou Y, Guo Y (2023) High selective removal towards Hg (II) from aqueous solution with magnetic diatomite-based adsorbent functionalized by poly (3-aminothiophenol): conditional optimization, application, and mechanism. Environ Sci Pollut Res 30(19):56121–56136
31. Lin Z, Pan Z, Zhao Y, Qian L, Shen J, Xia K, Guo Y, Qu Z (2020) Removal of Hg^{2+} with polypyrrole-functionalized Fe_3O_4/kaolin: synthesis, performance and optimization with response surface methodology. Nanomaterials 10(7):1370
32. S. Sireesha, I. Sreedhar 2023 Holistic and parametric optimization study on Cr (VI) removal using acid-treated coco peat biochar adsorbent, Bioresource Technology Reports 101486
33. Varghese SM, Chowdhury AR, Arnepalli DN, Rao GR (2023) Delineating the effects of pore structure and N-doping on CO_2 adsorption using coco peat derived carbon. Carbon Trends 10:100250
34. Peer FE, Bahramifar N, Younesi H (2018) Removal of Cd (II), Pb (II) and Cu (II) ions from aqueous solution by polyamidoamine dendrimer grafted magnetic graphene oxide nanosheets. J Taiwan Inst Chem Eng 87:225–240
35. Venkateswarlu S, Yoon M, Kim MJ (2022) An environmentally benign synthesis of Fe_3O_4 nanoparticles to Fe_3O_4 nanoclusters: rapid separation and removal of Hg (II) from an aqueous medium. Chemosphere 286:131673
36. Yang L, Wang Z, Yang L, Li X, Zhang Y, Lu C (2017) Coco peat powder as a source of magnetic sorbent for selective oil–water separation. Ind Crops Prod 101:1–10
37. Okoli CP, Naidoo EB, Ofomaja AE (2018) Role of synthesis process variables on magnetic functionality, thermal stability, and tetracycline adsorption by magnetic starch nanocomposite. Environ Nanotechnol Monit Manag 9:141–153
38. Bunaciu AA, UdriŞTioiu EG, Aboul-Enein HY (2015) X-ray diffraction: instrumentation and applications. Crit Rev Anal Chem 45(4):289–299
39. Verma S, Kujur S, Sharma R, Pathak DD (2022) Cucurbit [6] uril-supported Fe_3O_4 magnetic nanoparticles catalyzed green and sustainable synthesis of 2-substituted benzimidazoles via acceptorless dehydrogenative coupling. ACS Omega 7(11):9754–9764
40. Tan YH, Davis JA, Fujikawa K, Ganesh NV, Demchenko AV, Stine KJ (2012) Surface area and pore size characteristics of nanoporous gold subjected to thermal, mechanical, or surface modification studied using gas adsorption isotherms, cyclic voltammetry, thermogravimetric analysis, and scanning electron microscopy. J Mater Chem 22(14):6733–6745
41. Ncibi M, Jeanne-Rose V, Mahjoub B, Jean-Marius C, Lambert J, Ehrhardt J, Bercion Y, Seffen M, Gaspard S (2009) Preparation and characterisation of raw chars and physically activated carbons derived from marine Posidonia oceanica (L.) fibres. J Hazard Mater 165(1–3):240–249
42. Fu H, Yan D, Yao C, Su X, Wang X, Wang H, Li Y (2022) Pore structure and multi-scale fractal characteristics of adsorbed pores in marine shale: a case study of the Lower Silurian Longmaxi shale in the Sichuan Basin China. J Earth Sci 33(5):1278–1290
43. Kianfar E (2018) Synthesis and characterization of $AlPO_4$/ZSM-5 catalyst for methanol conversion to dimethyl ether. Russ J Appl Chem 91(10):1711–1720

44. Mangi HN, Chi R, DeTian Y, Sindhu L, He D, Ashraf U, Fu H, Zixuan L, Zhou W, Anees A (2022) The ungrind and grinded effects on the pore geometry and adsorption mechanism of the coal particles. J Nat Gas Sci Eng 100:104463
45. Ebadi M, Rifqi Md Zain A, Tengku Abdul Aziz TH, Mohammadi H, Tee CA, Rahimi Yusop M (2023) Formulation and characterization of Fe_3O_4@ PEG nanoparticles loaded sorafenib; molecular studies and evaluation of cytotoxicity in liver cancer cell lines. Polymers 15(4):971
46. Ma Z, Liu F, Liu N, Liu W, Tong M (2021) Facile synthesis of sulfhydryl modified covalent organic frameworks for high efficient Hg (II) removal from water. J Hazard Mater 405:124190
47. Einollahipeer F, Okati N (2022) High efficient Hg (II) and TNP removal by NH_2 grafted magnetic graphene oxide synthesized from Typha latifolia. Environ Technol 43(25):3956–3972
48. Ahmad M, Wang J, Xu J, Yang Z, Zhang Q, Zhang B (2020) Novel synthetic method for magnetic sulphonated tubular trap for efficient mercury removal from wastewater. J Colloid Interface Sci 565:523–535
49. Ge H, Hua T, Wang J (2017) Preparation and characterization of poly (itaconic acid)-grafted crosslinked chitosan nanoadsorbent for high uptake of Hg^{2+} and Pb^{2+}. Int J Biol Macromol 95:954–961
50. Das S, Samanta A, Kole K, Gangopadhyay G, Jana S (2020) MnO_2 flowery nanocomposites for efficient and fast removal of mercury (II) from aqueous solution: a facile strategy and mechanistic interpretation. Dalton Trans 49(20):6790–6800
51. Zhang Z, Xia K, Pan Z, Yang C, Wang X, Zhang G, Guo Y, Bai R (2020) Removal of mercury by magnetic nanomaterial with bifunctional groups and core-shell structure: synthesis, characterization and optimization of adsorption parameters. Appl Surf Sci 500:143970
52. Awad FS, AbouZied KM, Abou El-Maaty WM, El-Wakil AM, El-Shall MS (2020) Effective removal of mercury (II) from aqueous solutions by chemically modified graphene oxide nanosheets. Arab J Chem 13(1):2659–2670
53. Khorshidi P, Shirazi RHSM, Miralinaghi M, Moniri E, Saadi S (2020) Adsorptive removal of mercury (II), copper (II), and lead (II) ions from aqueous solutions using glutathione-functionalized $NiFe_2O_4$/graphene oxide composite. Res Chem Intermed 46:3607–3627
54. Falahian Z, Torki F, Faghihian H (2018) Synthesis and application of polypyrrole/Fe_3O_4 nanosize magnetic adsorbent for efficient separation of Hg^{2+} from aqueous solution. Global Chall 2(1):1700078
55. Asasian N, Kaghazchi T, Soleimani M (2012) Elimination of mercury by adsorption onto activated carbon prepared from the biomass material. J Ind Eng Chem 18(1):283–289
56. Naushad M, Ahamad T, AlOthman ZA, Ala'a H (2019) Green and eco-friendly nanocomposite for the removal of toxic Hg (II) metal ion from aqueous environment: adsorption kinetics & isotherm modelling. J Mol Liq 279:1–8
57. Ifthikar J, Jiao X, Ngambia A, Wang T, Khan A, Jawad A, Xue Q, Liu L, Chen Z (2018) Facile one-pot synthesis of sustainable carboxymethyl chitosan–sewage sludge biochar for effective heavy metal chelation and regeneration. Biores Technol 262:22–31
58. Xia K, Guo Y, Shao Q, Zan Q, Bai R (2019) Removal of mercury (II) by EDTA-functionalized magnetic $CoFe_2O_4$@ SiO_2 nanomaterial with core-shell structure. Nanomaterials 9(11):1532
59. Huang S, Ma C, Liao Y, Min C, Du P, Jiang Y (2016) Removal of mercury (II) from aqueous solutions by adsorption on poly (1-amino-5-chloroanthraquinone) nanofibrils: equilibrium, kinetics, and mechanism studies. J Nanomater 2016:7245829
60. Mensah MB, Lewis DJ, Boadi NO, Awudza JA (2021) Heavy metal pollution and the role of inorganic nanomaterials in environmental remediation. R Soc Open Sci 8(10):201485
61. Rahmanzadeh L, Ghorbani M, Jahanshahi M (2016) Effective removal of hexavalent mercury from aqueous solution by modified polymeric nanoadsorbent. J Water Environ Nanotechnol 1(1):1–8
62. AlOmar MK, Alsaadi MA, Jassam TM, Akib S, Hashim MA (2017) Novel deep eutectic solvent-functionalized carbon nanotubes adsorbent for mercury removal from water. J Colloid Interface Sci 497:413–421
63. Tabatabaiee Bafrooee AA, Ahmad Panahi H, Moniri E, Miralinaghi M, Hasani AH (2020) Removal of Hg^{2+} by carboxyl-terminated hyperbranched poly (amidoamine) dendrimers grafted superparamagnetic nanoparticles as an efficient adsorbent. Environ Sci Pollut Res 27:9547–9567
64. Zhang Y, Yan L, Xu W, Guo X, Cui L, Gao L, Wei Q, Du B (2014) Adsorption of Pb (II) and Hg (II) from aqueous solution using magnetic $CoFe_2O_4$-reduced graphene oxide. J Mol Liq 191:177–182
65. Cui L, Guo X, Wei Q, Wang Y, Gao L, Yan L, Yan T, Du B (2015) Removal of mercury and methylene blue from aqueous solution by xanthate functionalized magnetic graphene oxide: sorption kinetic and uptake mechanism. J Colloid Interface Sci 439:112–120
66. Goci MC, Leudjo Taka A, Martin L, Klink MJ (2023) Chitosan-based polymer nanocomposites for environmental remediation of mercury pollution. Polymers 15(3):482
67. Liu F, Liu Y, Xu Y, Ni L, Meng X, Hu Z, Zhong G, Meng M, Wang Y, Han J (2015) Efficient static and dynamic removal of Sr (II) from aqueous solution using chitosan ion-imprinted polymer functionalized with dithiocarbamate. J Environ Chem Eng 3(2):1061–1071
68. Zhao R, Jia L, Yao Y-X, Huo R-P, Qiao X-L, Fan B-G (2019) Study of the effect of adsorption temperature on elemental mercury removal performance of iron-based modified biochar. Energy Fuels 33(11):11408–11419
69. Johari K, Saman N, Song ST, Cheu SC, Kong H, Mat H (2016) Development of coconut pith chars towards high elemental mercury adsorption performance–effect of pyrolysis temperatures. Chemosphere 156:56–68
70. Fuente-Cuesta A, Diaz-Somoano M, Lopez-Anton M, Cieplik M, Fierro J, Martínez-Tarazona M (2012) Biomass gasification chars for mercury capture from a simulated flue gas of coal combustion. J Environ Manage 98:23–28
71. Safari N, Ghanemi K, Buazar F (2020) Selenium functionalized magnetic nanocomposite as an effective mercury (II) ion scavenger from environmental water and industrial wastewater samples. J Environ Manage 276:111263
72. Bhatnagar P, Sireesha S, Siddiqui S, Sreedhar I (2023) Novel pectin-cellulose-biochar composite with SDS modification for copper removal: optimization, characterization, and regeneration. Bioresour Technol Rep 21:101382
73. Samaniego JO, Tanchuling MAN (2019) Removal of heavy metals from an actual small scale gold mining wastewater by sorption onto Cocopeat. ASEAN J Sci Technol Dev 36(1):1–7
74. Hosseini-Bandegharaei A, Hosseini MS, Jalalabadi Y, Sarwghadi M, Nedaie M, Taherian A, Ghaznavi A, Eftekhari A (2011) Removal of Hg (II) from aqueous solutions using a novel impregnated resin containing 1-(2-thiazolylazo)-2-naphthol (TAN). Chem Eng J 168(3):1163–1173
75. Jena KK, Reddy KSK, Karanikolos GN, Choi DS (2023) l-Cysteine and silver nitrate based metal sulfide and Zeolite-Y nano adsorbent for efficient removal of mercury (II) ion from wastewater. Appl Surf Sci 611:155777
76. Arshadi M, Mousavinia F, Khalafi-Nezhad A, Firouzabadi H, Abbaspourrad A (2017) Adsorption of mercury ions from wastewater by a hyperbranched and multi-functionalized dendrimer modified mixed-oxides nanoparticles. J Colloid Interface Sci 505:293–306

77. Chen F, Ma N, Peng G, Xu W, Zhang Y, Meng F, Huang Q, Hu B, Wang Q, Guo X (2023) *Camellia oleifera* shell biochar as a robust adsorbent for aqueous mercury removal. Fermentation 9(3):295
78. Esrafili A, Ghambarian M, Tajik M, Baharfar M (2020) Adsorptive removal of Hg^{2+} from environmental water samples using thioglycerol-intercalated magnetic layered double hydroxides. Anal Methods 12(17):2279–2286
79. Hadi P, To M-H, Hui C-W, Lin CSK, McKay G (2015) Aqueous mercury adsorption by activated carbons. Water Res 73:37–55
80. Sun X, Hwang J-Y, Xie S (2011) Density functional study of elemental mercury adsorption on surfactants. Fuel 90(3):1061–1068
81. Duan L, Hu X, Sun D, Liu Y, Guo Q, Zhang T, Zhang B (2020) Rapid removal of low concentrations of mercury from wastewater using coal gasification slag. Korean J Chem Eng 37:1166–1173